Supplement of Atmos. Chem. Phys., 24, 4827–4850, 2024
https://doi.org/10.5194/acp-24-4827-2024-supplement

Supplement of

Extreme ozone episodes in a major Mediterranean urban area

Jordi Massagué et al.

Correspondence to: Jordi Massagué (jordi.massague@idaea.csic.es)

Contents

S1. 2015 episode (6 June)

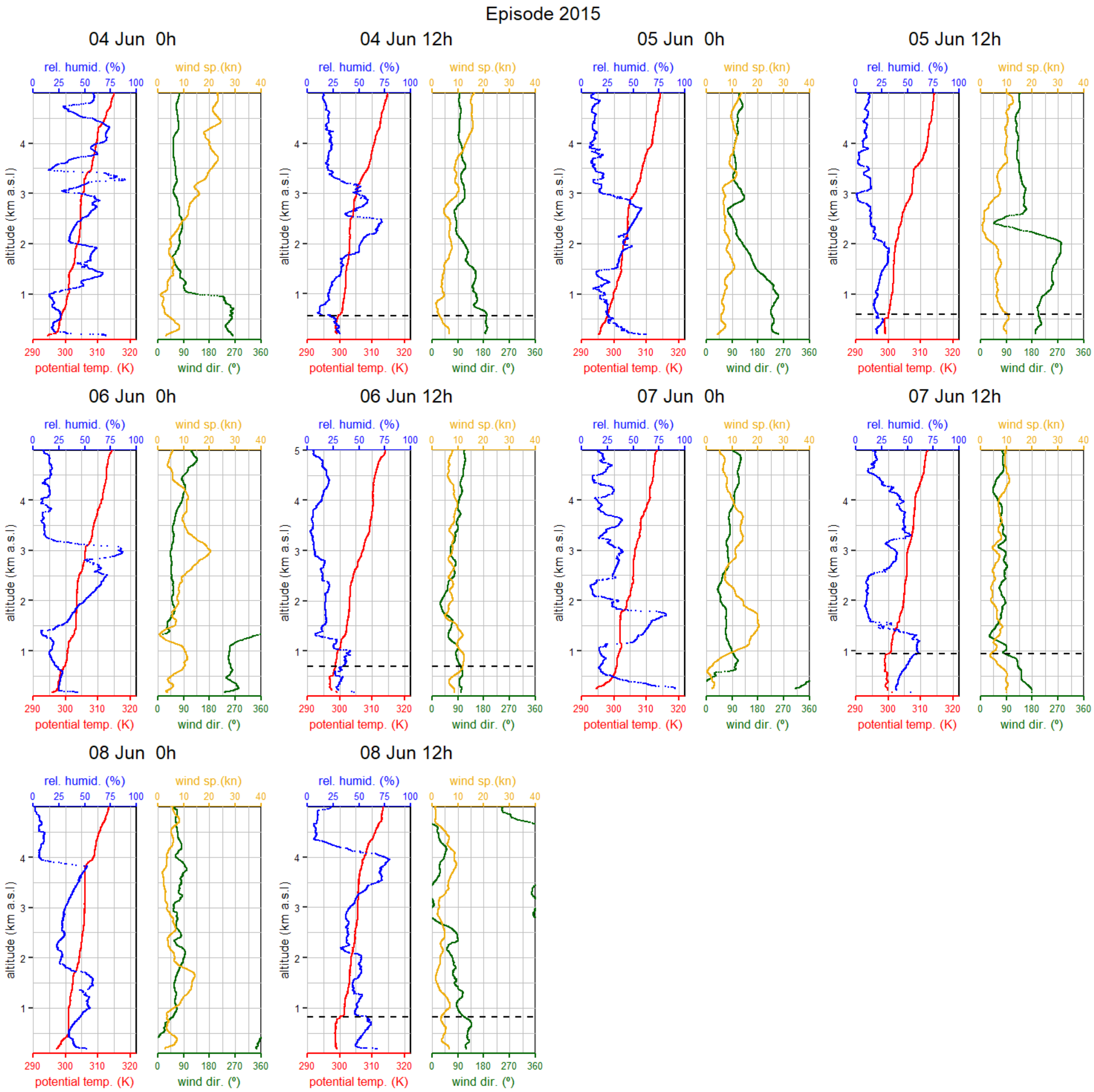

Figure S1. Radiosonde data (2015 episode). Midnight and midday potential temperature, relative humidity, wind direction and speed in Barcelona (0–5,000 m above sea level). Horizontal dotted lines, representing mixing layer height (MLH), are shown exclusively for noon data.

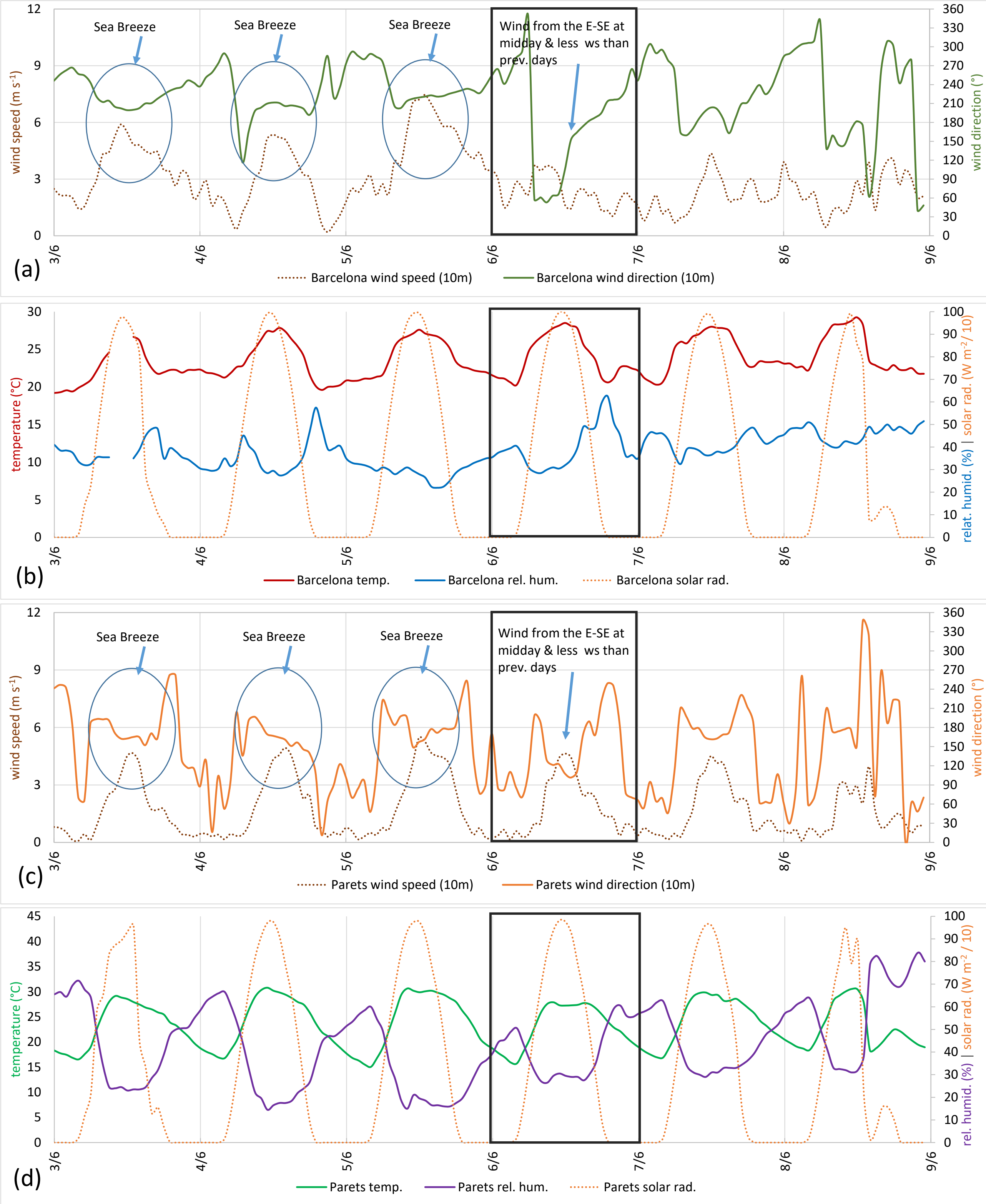

Figure S2. Surface meteorological parameters (2015 episode). (a): Barcelona wind speed and direction (10 m above ground level (AGL)), (b) Barcelona temperature, relative humidity, solar radiation. (c) Parets (25 km northward, downwind of Barcelona) wind speed and direction (10 m AGL) and (d) Parets temperature, relative humidity, solar radiation.

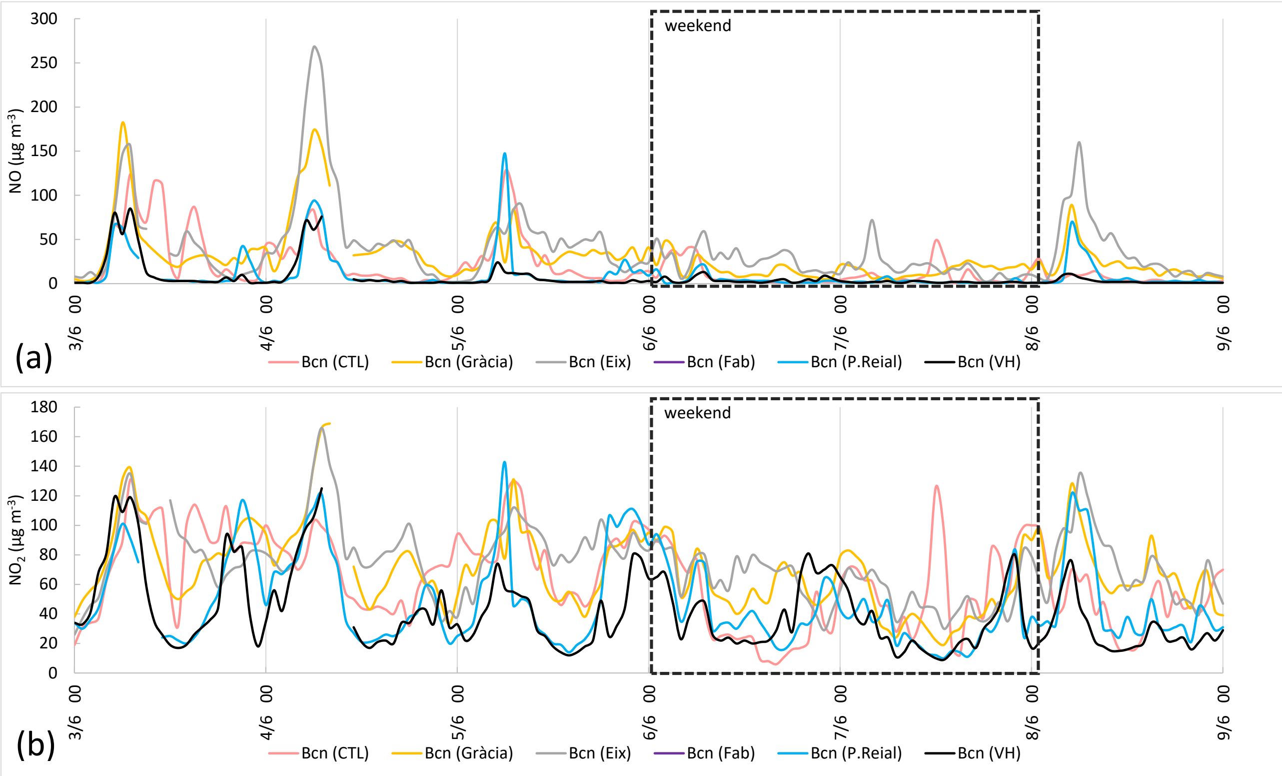

Figure S3. (a) NO and (b) NO_2 concentrations observed in Barcelona during the 2015 episode. A decrease in the NOx concentrations is evident during the weekend.

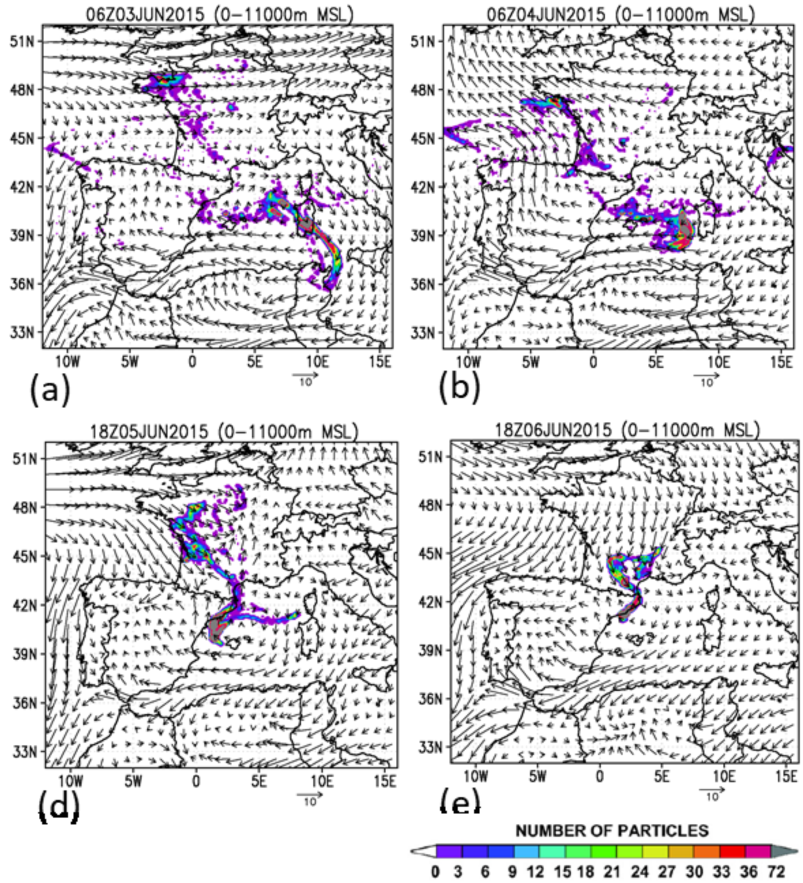

Figure S4. Episode 2015. RAMS/HYPACT back-trajectories of arrival in Barcelona (Ciutadella) the 6 (day of episode) and 7 June. Vectors are average wind from 0–1,000 m AGL (sigma levels), and the shaded areas represent the total number of particles accumulated on the vertical of the site. (a–d) Crossing the Western Mediterranean with east and southeast winds during June 3–5, and from France with west winds on the 5 June. (e, f) From the South, along the East coast of Spain (Mediterranean influence) with the Mediterranean Gyre circulation, and from the North, through the Gulf of Lion, sweeping the south of France.

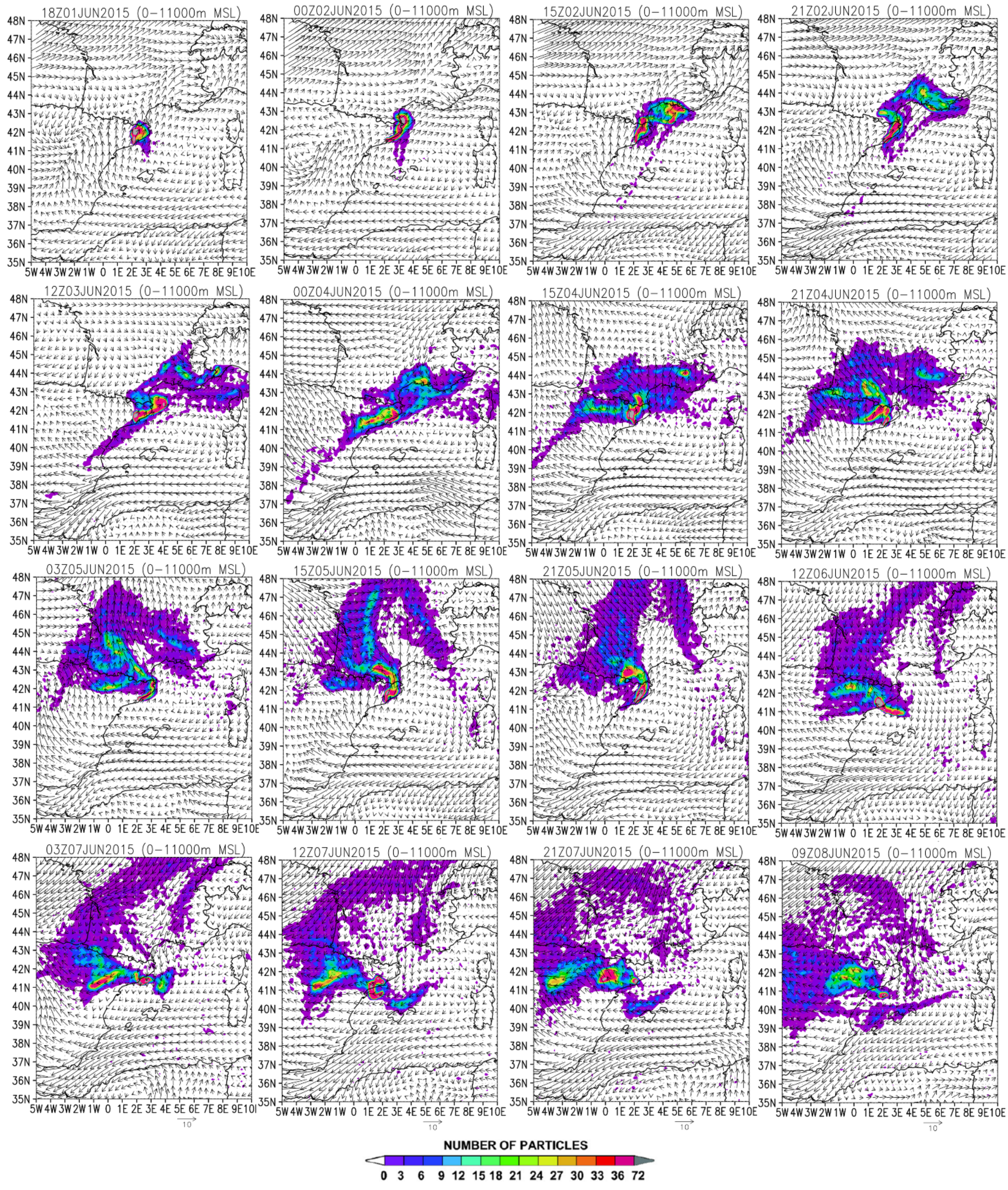

Figure S5. Dispersion sequence of the Barcelona plume (emitted from the centre of the city) along with the average wind field at 0–800 m AGL, which explains the transport pattern. Before June 6, the transport is directed northward, and there is no recirculation (sea-land) of the emissions. On and after June 6 (coinciding with the Tramontana winds), there is sea-land recirculation along the Barcelona coast. The plume completes a full rotation every day, and Barcelona is situated at the centre of a convergence zone for airflows coming from the Gulf of Lion. These airflows move southward parallel to the coast during the night and merge with the emissions from the south and southeast, influenced by sea breezes and the Mediterranean circulation.

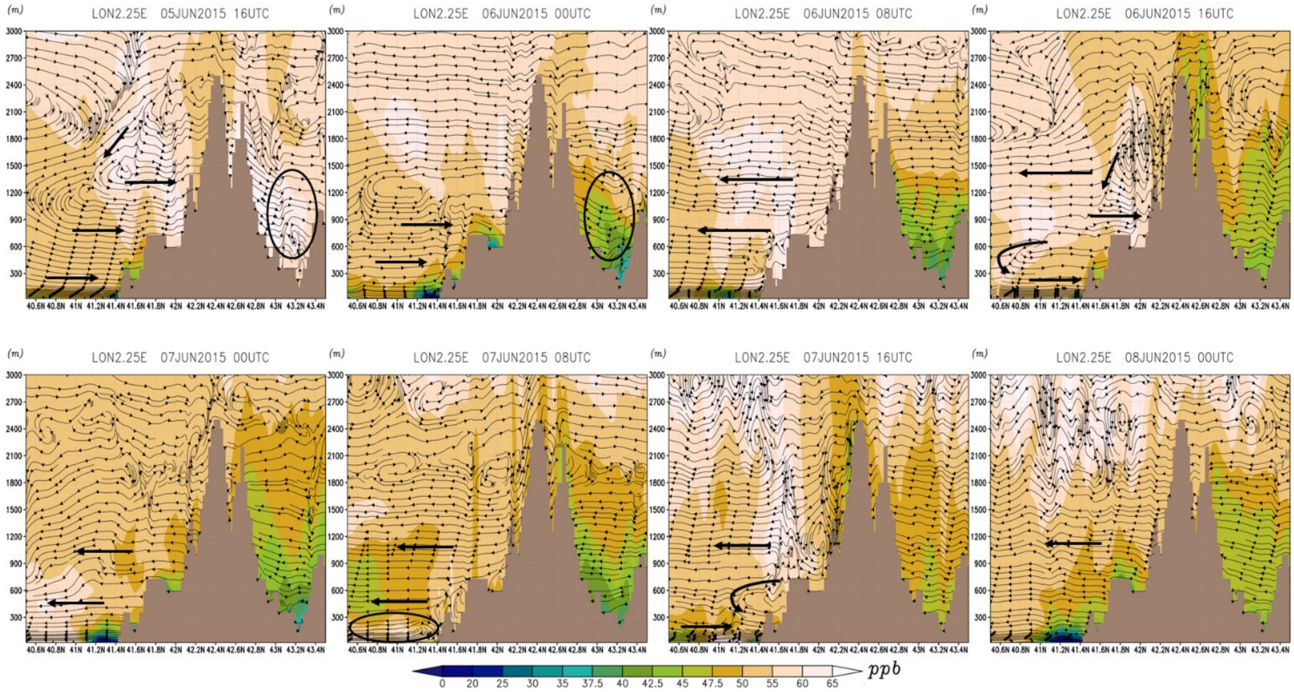

Figure S6. Episode 2015. Simulated O_3 along the cross section Barcelona-Vic. Horizontal winds projected together with vertical winds. Concentrations are shown in ppb since they are altitude independent (1 ppb ≈ 2 $\mu g \cdot m^{-3}$ at sea level).

S2. 2018 episode (4 and 5 August)

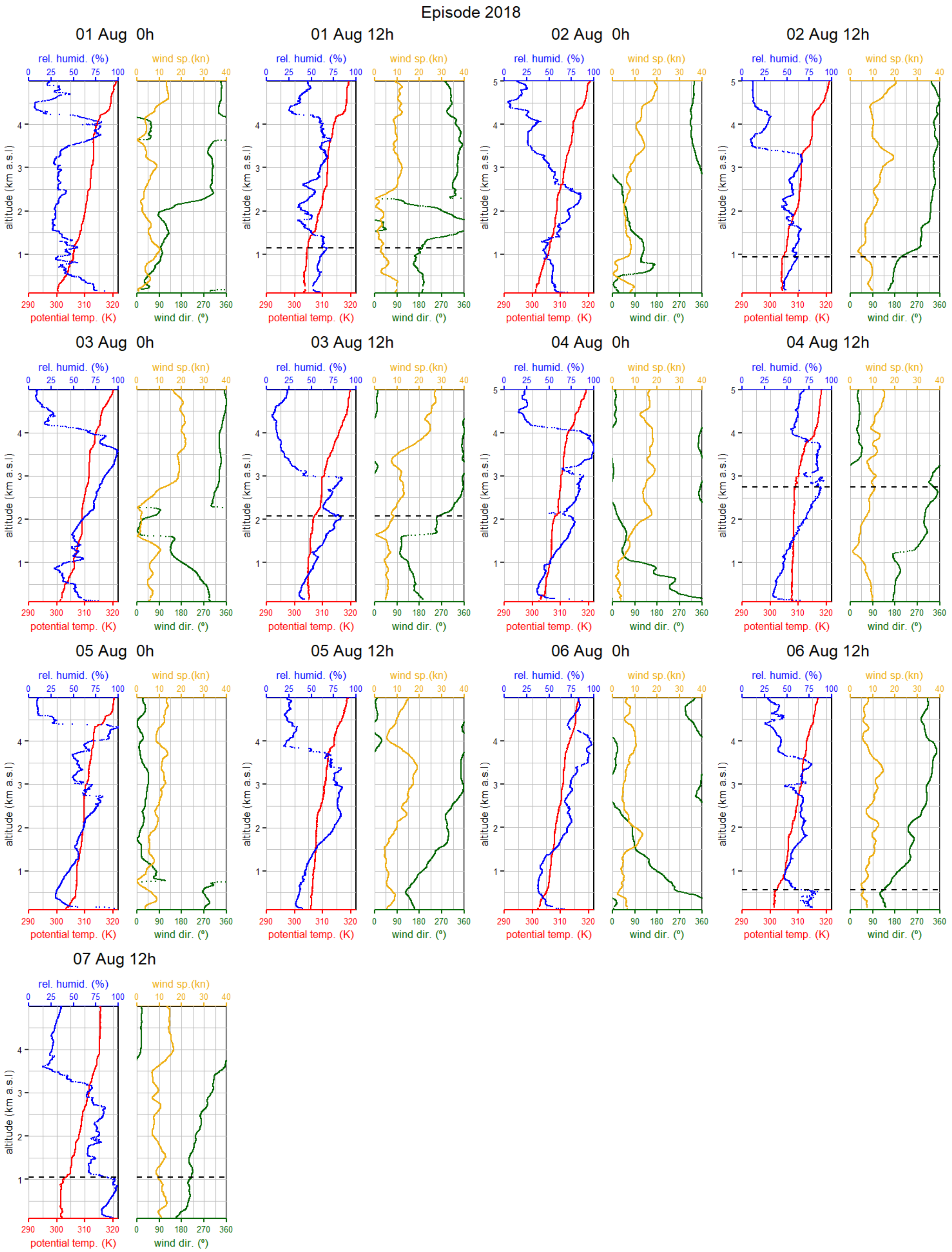

Figure S7. Radiosonde data (2018 episode). Midnight and midday potential temperature, relative humidity, wind direction and speed in Barcelona for 0–5,000 m above sea level. Horizontal dotted lines, representing mixing layer height (MLH), are shown exclusively for noon data. Some are missing due to technical issues. No radiosonde data for the night of the 7 August.

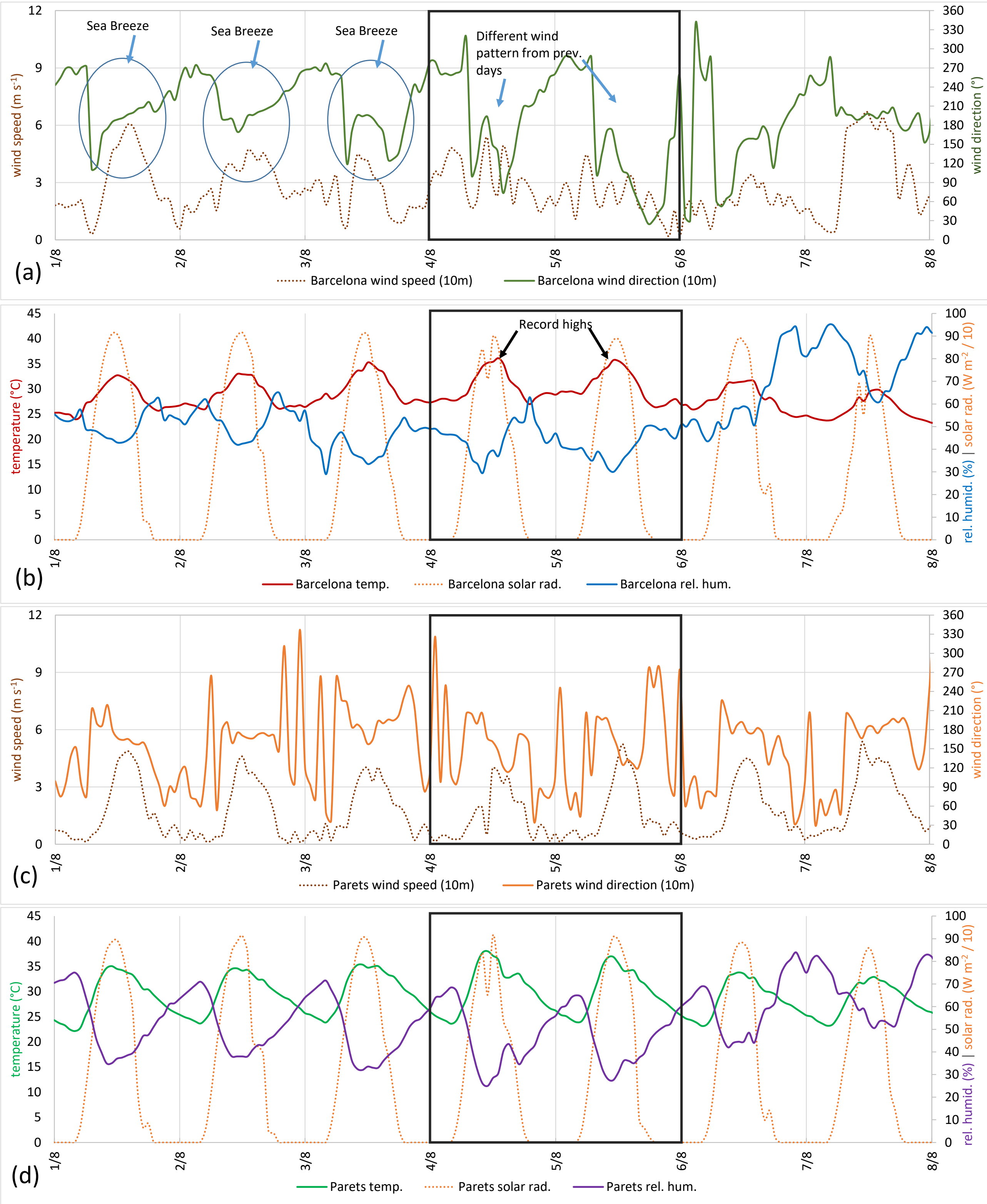

Figure S8. Surface meteorological parameters (2018 episode). (a): Barcelona wind speed and direction (10 m above ground level (AGL)), (b) Barcelona temperature, relative humidity, solar radiation. (c) Parets (25 km downwind of Barcelona) wind speed and direction (10 m AGL) and (d) Parets temperature, relative humidity, solar radiation.

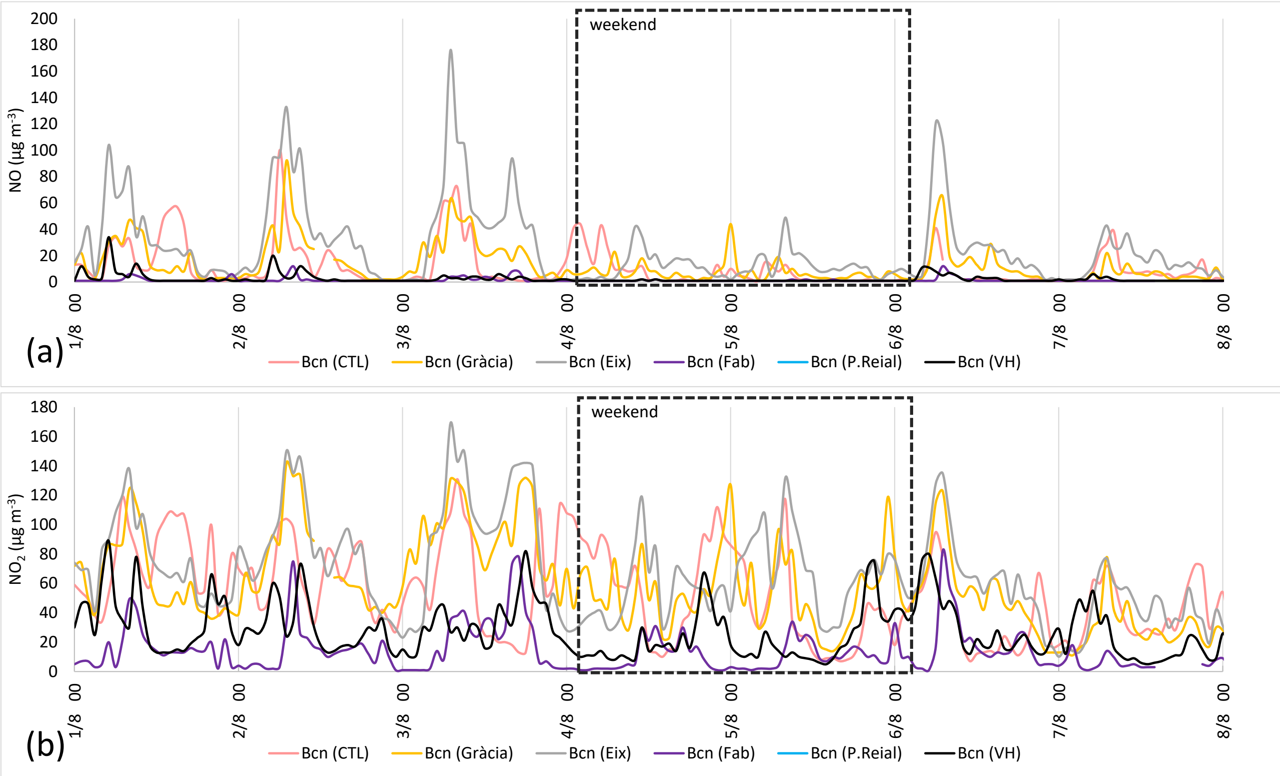

Figure S9. (a) NO and (b) NO_2 concentrations observed in Barcelona during the 2018 episode. A decrease in the NOx concentrations is evident during the weekend.

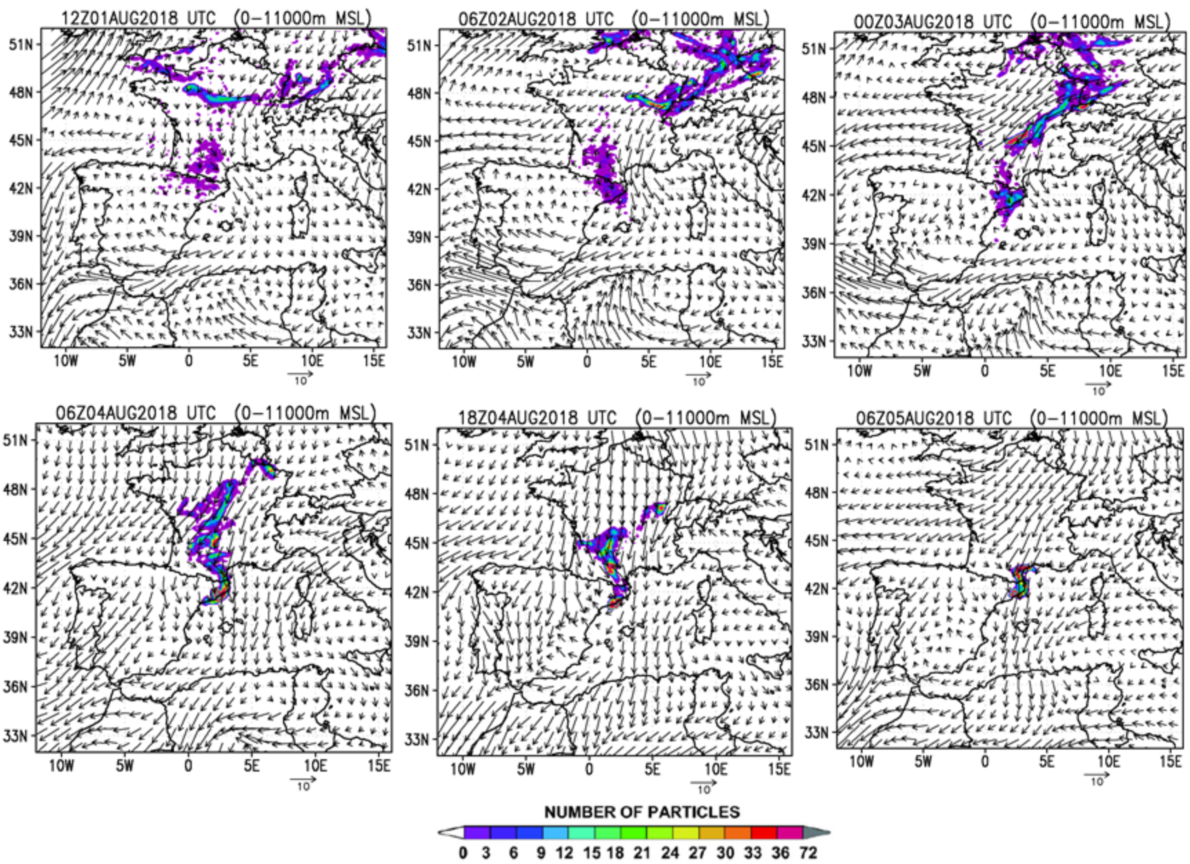

Figure S10. Episode 2018. RAMS/HYPACT back-trajectories of arrival in Barcelona (Fabra) the 4 and 5 of August 2018 (days of episode). Vectors are average wind from 0–1,000 m AGL (sigma levels), and the shaded areas represent the total number of particles accumulated on the vertical of the site. Top row, before the episode, bottom row during the episode.

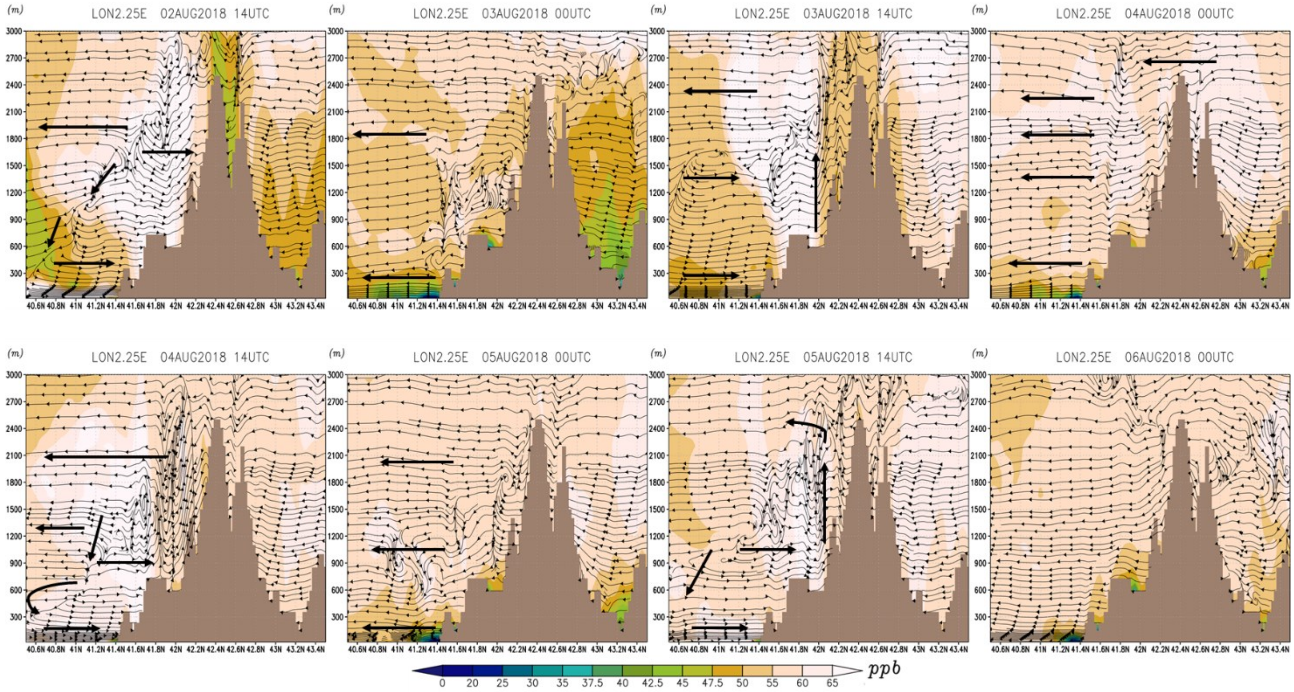

Figure S11. Episode 2018. Simulated O_3 along the cross section Barcelona-Vic. Horizontal winds projected together with vertical winds. Concentrations are shown in ppb since they are altitude independent (1 ppb ≈ 2 $\mu g \cdot m^{-3}$ at sea level).

S3. 2019 episode (29 June)

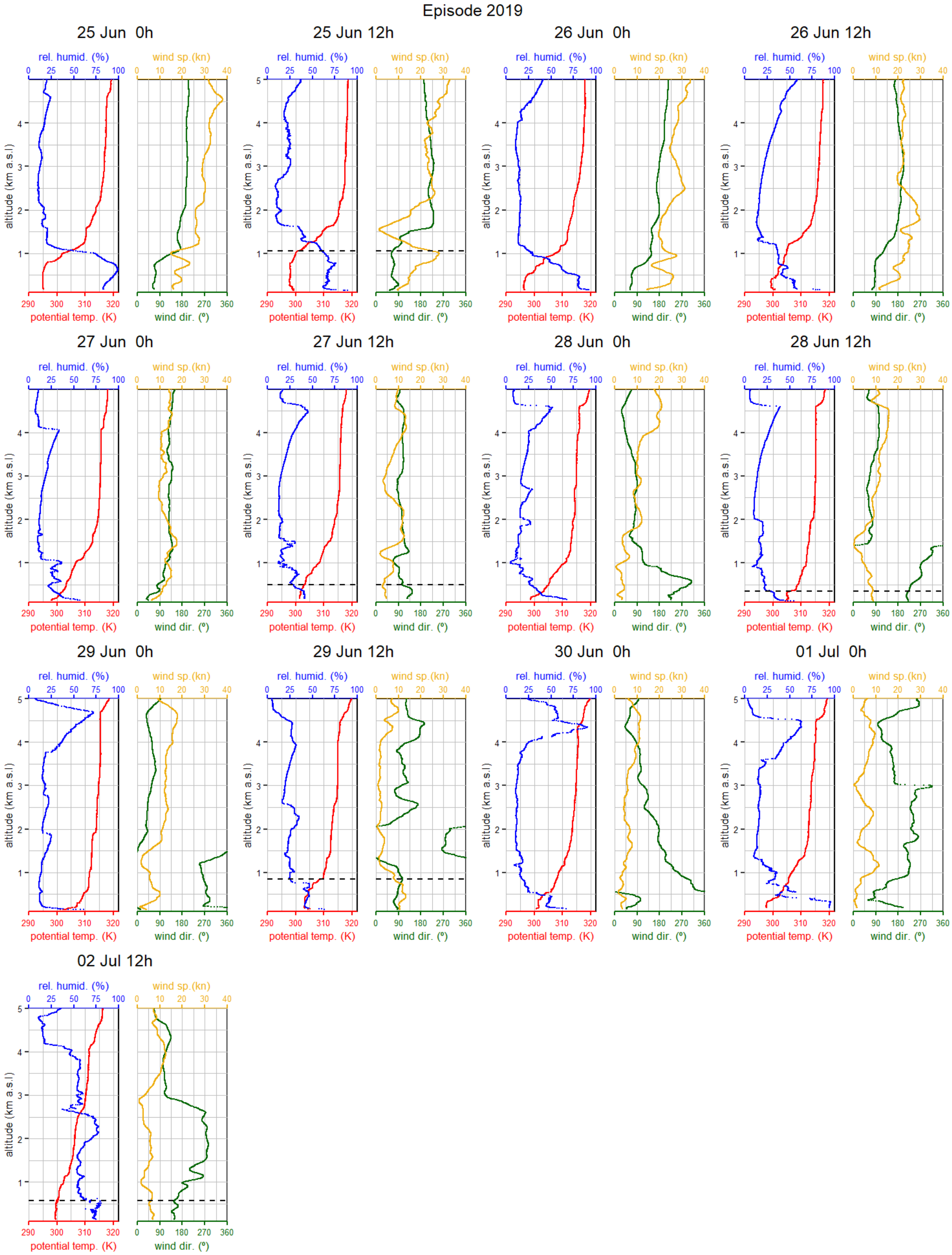

Figure S12. Radiosonde data (2019 episode). Midnight and midday potential temperature, relative humidity, wind direction and speed in Barcelona for 0–5,000 m above sea level. Horizontal dotted lines, representing mixing layer height (MLH), are shown exclusively for noon data. Some are missing due to technical issues. No radiosonde data for the midday of 30 June, 1 July, and for the night of the 2 July.

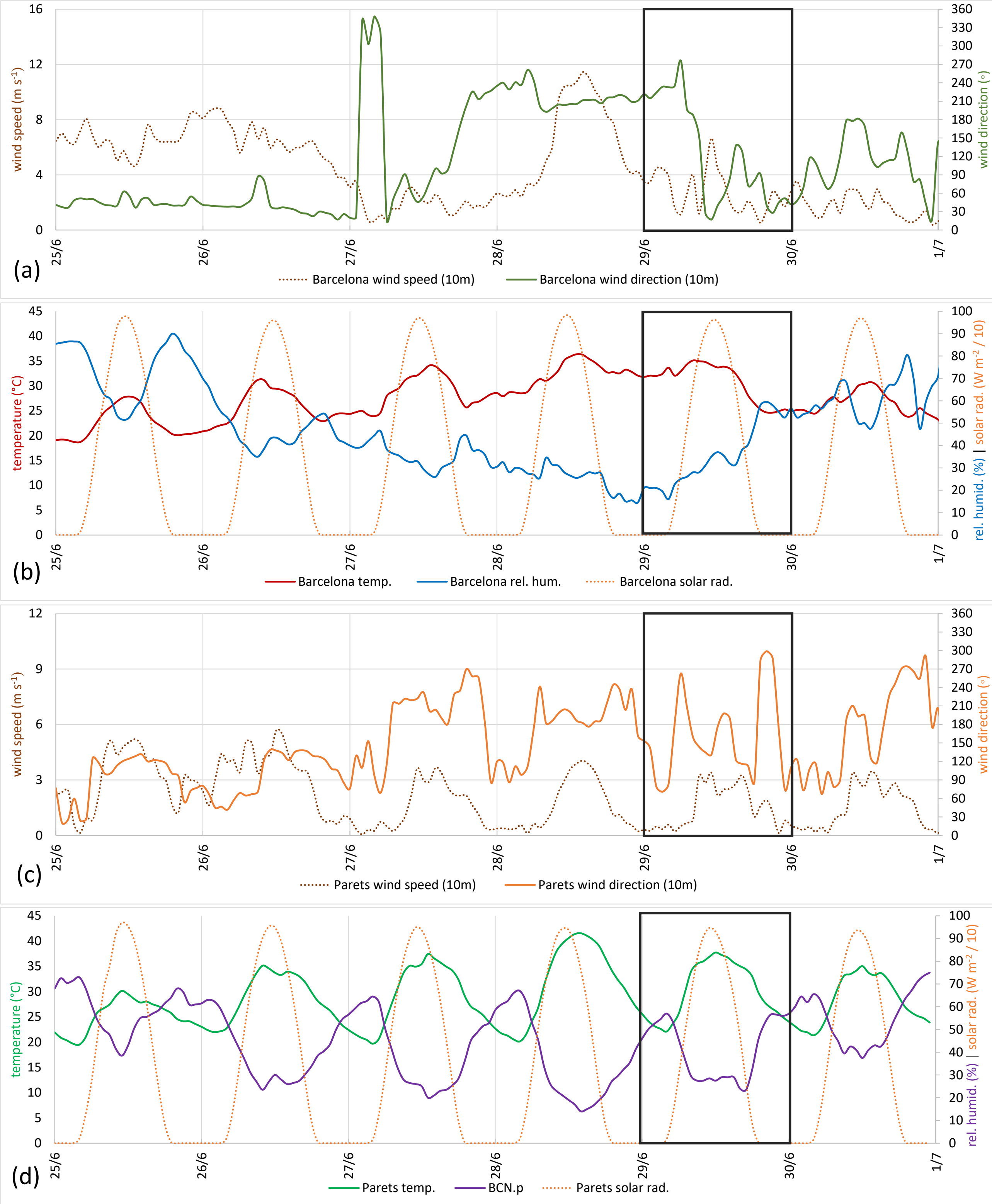

Figure S13. Surface meteorological parameters during (2019 episode). (a): Barcelona wind speed and direction (10 m above ground level (AGL)). (b) Barcelona temperature, relative humidity, solar radiation. (c) Parets (25 km northward, downwind of Barcelona) wind speed and direction (10 m AGL) and (d) Parets temperature, relative humidity, solar radiation.

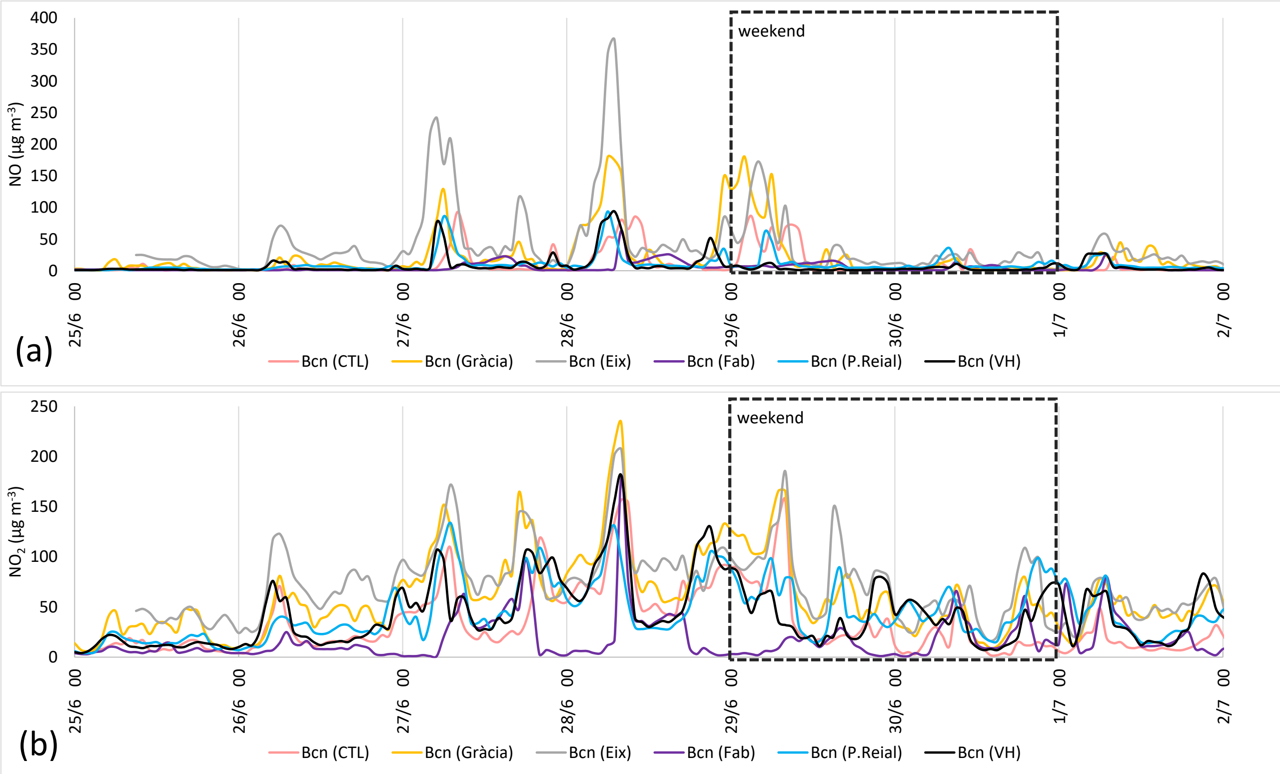

Figure S14. (a) NO and (b) NO_2 concentrations observed in Barcelona during the 2019 episode. A decrease in the NOx concentrations on the weekend is evident.

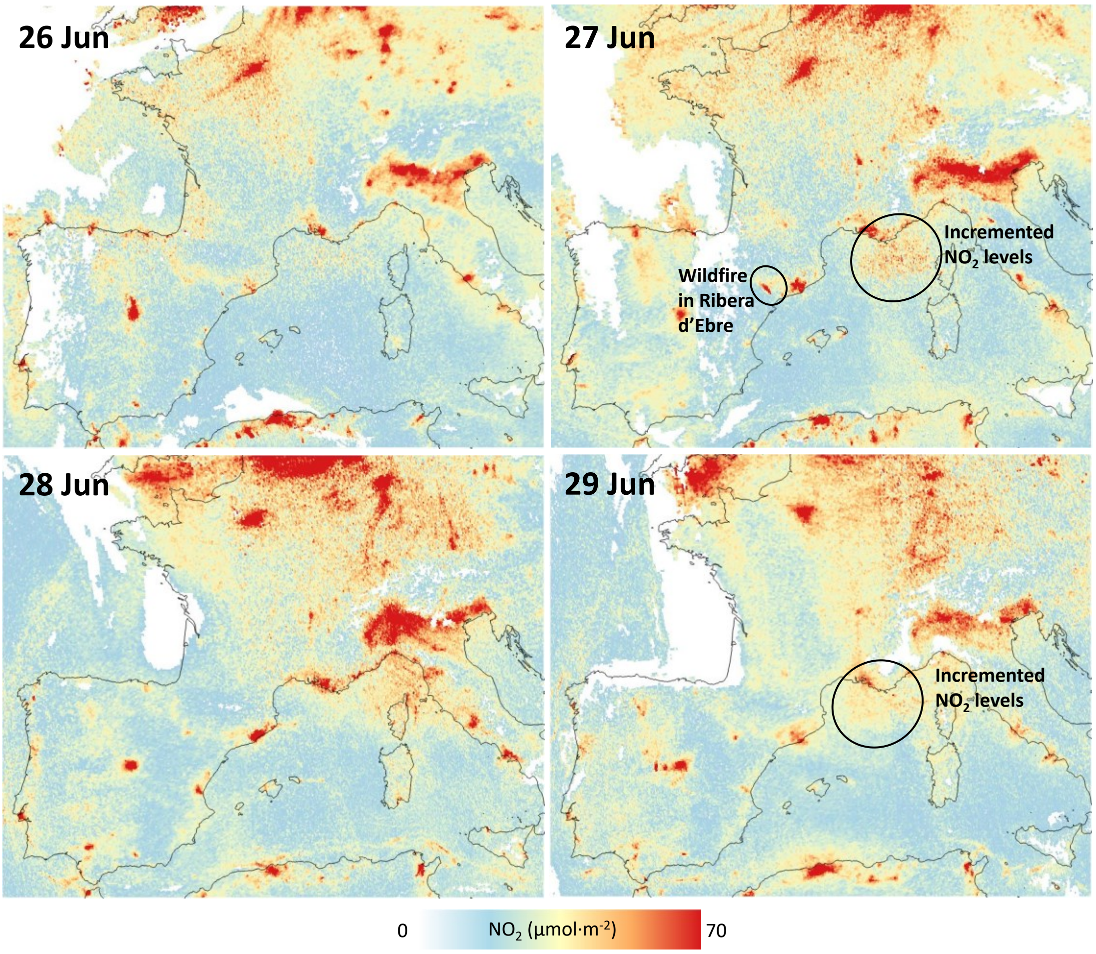

Figure S15. Tropospheric column NO_2 concentrations observed by TROPOMI–ESA during the 2019 episode.

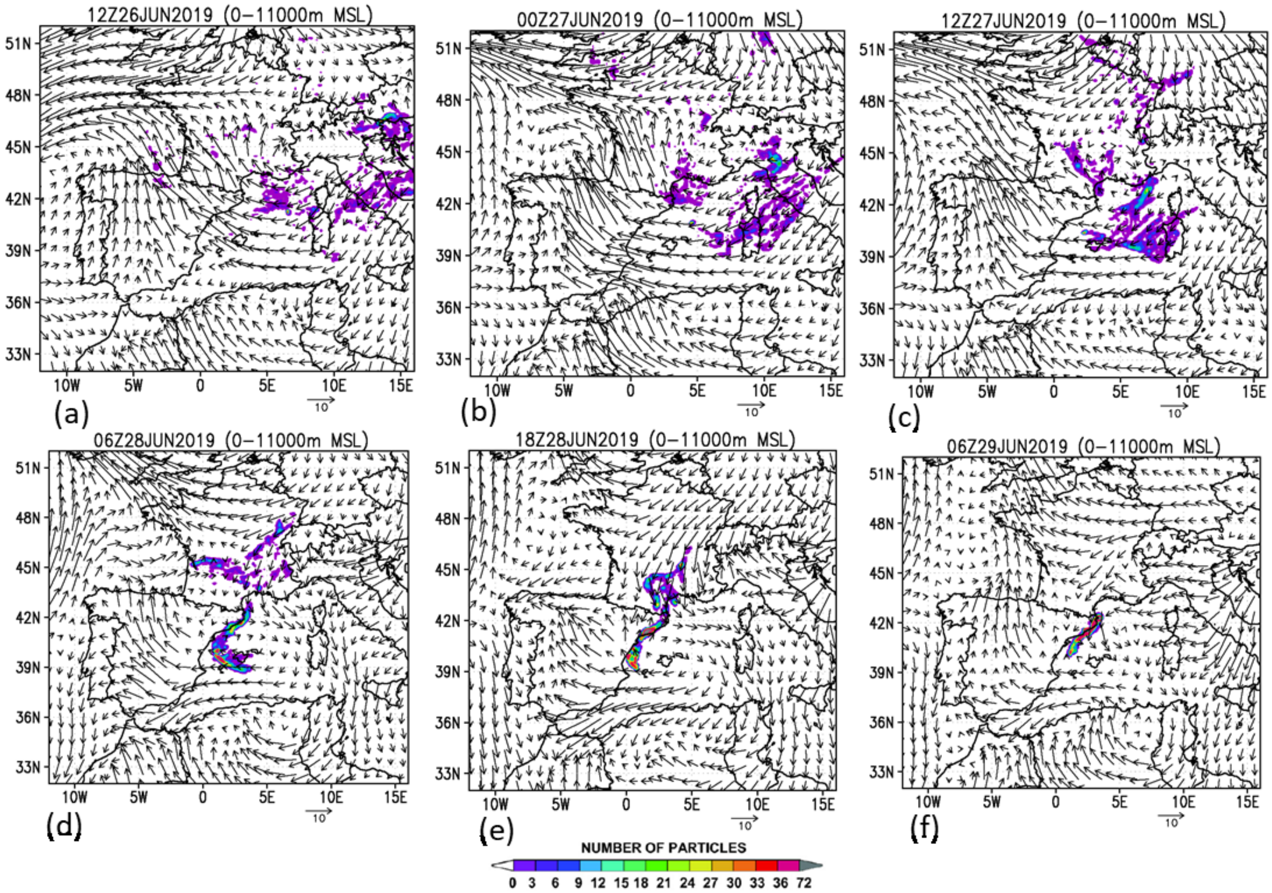

Figure S16. Episode 2019. RAMS/HYPACT back-trajectories of arrival in Barcelona (Fabra) the 29 of June (day of episode). Vectors are average wind from 0–1,000 m above ground level (AGL) (sigma levels), and the shaded areas represent the total number of particles accumulated on the vertical of the site. (a–c) Crossing the Western Mediterranean with east winds, and from central Europe with north winds. (d–f) From the south, following the coast (Mediterranean inputs) with the circulation of the Mediterranean Gyre, and from the north, with a characteristic entry through the Gulf of Lion, sweeping across southern France (continental Europe contributions).

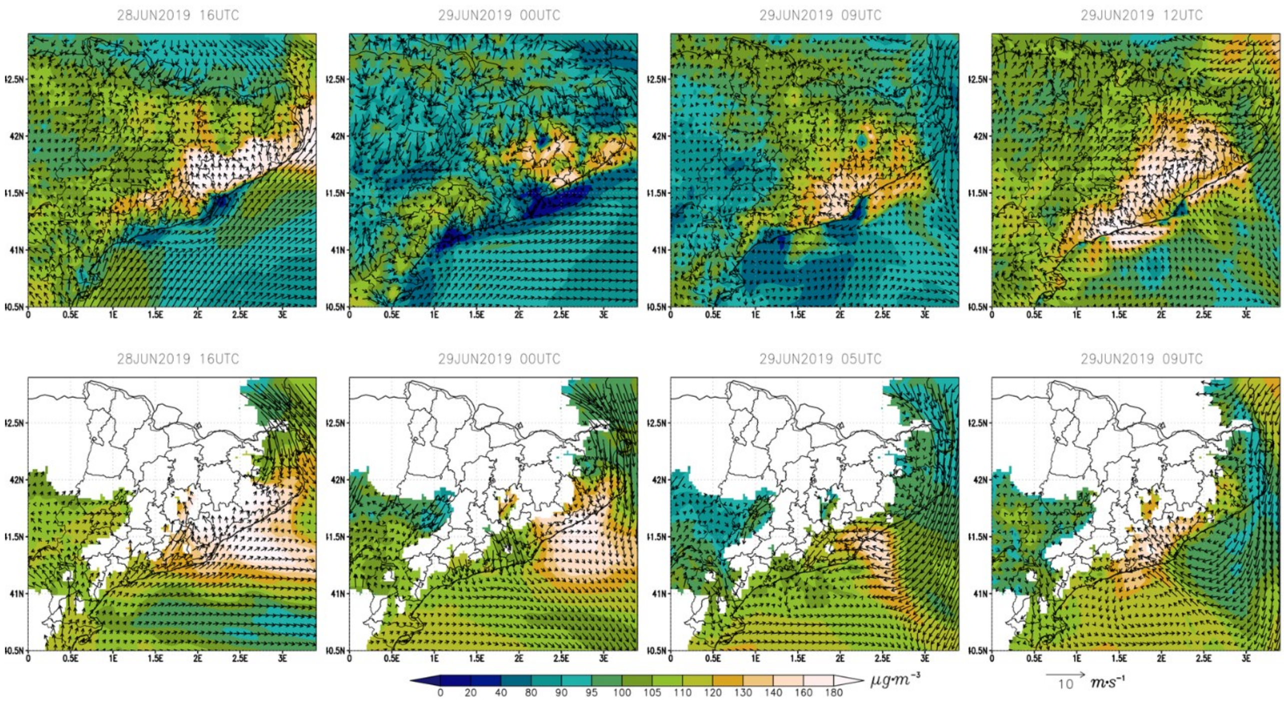

Figure S17. Episode 2019. (Top row) Simulated O_3 concentrations (colour scale, $\mu g{\cdot}m^{-3}$) and average wind fields (vectors, $m{\cdot}s^{-1}$) at (top row) surface level and (bottom row) at 600 m above ground level.

S4. Preliminary estimations of ozone contributions during the episodes

This section complements the concluding section of the main manuscript (Section 4) by detailing the process involved in estimating various contributions of O_3 that potentially contributed to the abnormally high concentrations during the episodes in Barcelona. As a general assumption, each estimated O_3 contribution (e.g., the O_3 contribution of the weekend effect) remains consistent across all episodes.

The estimations we propose here are based on the results of this study (see Section 3), and the variations in O_3 concentrations over consecutive days. To determine these variations, we graphically extracted O_3 concentration values from the central peak zone of each day (see diel variations in Figures 3b, 7b and 11b). We compared these values across consecutive days. Recognizing the considerable variability in O_3 levels among the six city stations, we specifically selected data from two to three stations for each episode. This selection aimed to capture representative O_3 levels in the city, deliberately excluding stations with extreme values—both higher and lower—in order to enhance the overall representativeness of the dataset for each specific episode.

For simplification, we grouped the different city sources identified in the trajectory analyses (see Sections 3.2.3, 3.3.3 and 3.4.3) into three major geographical source areas. These source areas include "North" encompassing sources from southern France (Toulouse, Montpellier, Marseille, etc.), entering the Mediterranean basin through the Gulf of Lion; "South" including sources from the Eastern Spanish coast (Tarragona, Castellón, Valencia, etc.); and "East", comprising sources from the interior of the Mediterranean located east of Barcelona (Palma, Cagliari, Rome, and even maritime traffic).

It is useful to mention potential implications that the Tramontana meteorological conditions (Gangoiti et al., 2001) may have within the context of this study. These "Tramontana conditions", consistently observed in all analysed episodes, are characterised by coastal breezes of lesser intensity than usual for the season, with coastal recirculations, upper-level winds favouring sea breeze overturning, and increased convergence of air masses over Barcelona. These convergences, which are a result of coastal circulations following the Lion jet, lead to diminished winds within the convergence zone. Notably, these conditions vary with each Tramontana instance due to the evolving jet stream and the variable recirculations in the wake zone between the jet stream and the Barcelona coast. These recirculations may, in turn, facilitate the transport of air masses from one or a combination of the source areas or regions mentioned above.

During the June 2015 episode, surface O_3 concentrations in Barcelona reached 80−110 $\mu g \cdot m^{-3}$ on Friday 5 (Figure 3b). According to the meteorological context detailed in Section 3.2.1, on this day there were no Tramontana conditions, nor convergence of air masses from multiple source areas (multiregional convergence), and the Besòs-axis dynamics (refer to Section 3.2.2) was well developed. Tramontana conditions began on Saturday 6 (episode in Barcelona), persisting until Tuesday 9. In this context, breezes were shorter than usual, confined to coastal areas, and the return was more favoured by the N-NW component of the Tramontana. On Saturday 6, the most significant O_3 contributions originated from the conjunction of the "South" (in this case, Tarragona) and "East" (mainly Palma, Cagliari) source areas (Figure 4a), resulting in O_3 concentrations reaching 160−180 $\mu g \cdot m^{-3}$. On Sunday 7, contributions were predominantly from the "North" area (Toulouse, Montpellier, Marseille), in contrast to the combined "South" and "East" contributions on the previous day, with concentrations reaching ~130 $\mu g \cdot m^{-3}$. On Monday 8, O_3 concentrations reached 110−120 $\mu g \cdot m^{-3}$ (Figure 3b).

Given the similar meteorological conditions to the preceding day, where the Besòs-axis dynamics had not restored, and contributions also came from the "North" area, albeit with a different distribution than on Sunday 7 (Toulouse had relatively lower contribution, and Montpellier a higher one), these contributions were assumed to be of the same magnitude as those of the previous day. Consequently, the difference between O_3 concentrations on Sunday 7, and Monday 8, is considered plausible to represent the weekend effect contribution (~15 $\mu g \cdot m^{-3}$).

The observed difference of ~75 $\mu g \cdot m^{-3}$ in O_3 concentrations between Friday 5 (without Tramontana conditions) and Saturday 6 (with Tramontana conditions), is likely attributable to the combined effects of contributions from both the "South" and "East" sources, alongside the weekend effect influencing Saturday 6. By subtracting the recently estimated weekend effect contribution (~15 $\mu g \cdot m^{-3}$) from this O_3 gradient, the cumulative contribution of the "South" and "East" during Tramontana-induced convergence is estimated to be ~60 $\mu g \cdot m^{-3}$ (75-15 $\mu g \cdot m^{-3}$). Similarly, the contribution from the "North" source area during Sunday 7 can be estimated by computing the difference in O_3 concentrations between this day and Friday 5, once again subtracting the weekend effect contribution. This results in an approximate ~20 $\mu g \cdot m^{-3}$ (130-15-95 $\mu g \cdot m^{-3}$) contribution from the "North" under Tramontana convergence conditions.

The estimations derived from the June 2015 episode can be tested to the June 2019 episode observed concentrations. As indicated in Section 3.4.1, Tramontana conditions occurred on Friday 28 and Saturday 29 (episode in Barcelona), and the difference between the O_3 levels on these two days was ~100 $\mu g \cdot m^{-3}$ (Figure 11b). On Friday 28, there was an influence from the "South" source area (mainly from Tarragona), concentrated in the early morning. However, this influence did not seem to affect O_3 levels during the central hours of the day, as indicated by the absence of any discernible trace in the city during these times (Figure 12b). On Saturday 29, contributions from all sources, including "North", "South" and "East", were combined (Figure 12b), resulting in the highest increase in O_3 on the episode day compared to the previous day among the three episodes. The cumulative estimated contributions for the 2015 episode, which include ~15 $\mu g \cdot m^{-3}$ from the weekend effect, combined contributions from "South" and "East" of ~60 $\mu g \cdot m^{-3}$, and the contribution "North", ~20 $\mu g \cdot m^{-3}$, add up to ~95 $\mu g \cdot m^{-3}$. Remarkably, this approximately aligns with the observed increase between Friday 28 and Saturday 29 during the 2019 episode. This alignment suggests that the estimated contributions for the 2015 episode could effectively explain O_3 contributions during the 2019 episode, providing support for the validity of the estimation methodology.

It is important to distinguish the contributions of O_3 transported from the "South" and "East" source areas which, based on the previous estimation, sum up to ~60 $\mu g \cdot m^{-3}$. In the August 2018 episode, Tramontana conditions prevailed on both the day before the episode (Friday 3), and the two days of the episode (Saturday 4 and Sunday 5) as outlined in Section 3.3.1. On Friday 3, where concentrations reached 120−130 $\mu g \cdot m^{-3}$ (Figure 7b), multiregional convergence was absent (Figure 8b), as the contribution was solely from the "North" source area (in this case, Toulouse). However, on Saturday 4, concentrations reached ~170−180 $\mu g \cdot m^{-3}$ (Figure 7b), with the occurrence of multiregional convergence. This involved contributions from an extensive area in central Europe (Stuttgart, Prague, etc.), in addition to a contribution from the "South" (mainly Tarragona) (Figure 8). The observed difference of ~50 $\mu g \cdot m^{-3}$ in surface concentrations in Barcelona between Friday 3 and the weekend could be attributed to the sum of the weekend effect contribution (~15 $\mu g \cdot m^{-3}$), the contribution from the "South", and an additional "new" multiregional contribution, not originating from the Marseille-Montpellier arc but from central Europe.

Given the observed "North" contribution on Friday 3 (Figure 8), an additional contribution of ~5−10 $\mu g \cdot m^{-3}$ is assumed to account for this central Europe contribution. Considering this adjustment, the estimated contribution from the "South" is ~25−30 $\mu g \cdot m^{-3}$. Subtracting this contribution from the combined "South" + "East" (60 $\mu g \cdot m^{-3}$) mentioned earlier, a contribution of ~30−35 $\mu g \cdot m^{-3}$ can be attributed to the "East" source area.

These estimations indicate high O_3 inputs from Mediterranean source areas "South" and "East" with somewhat smaller yet significant contributions from the "North", in addition to those attributed to the weekend effect:

- North (through the Gulf of Lion): 20 $\mu g \cdot m^{-3}$
- East (or interior Mediterranean sources): 30−35 $\mu g \cdot m^{-3}$
- South (Tarragona and other Spanish Mediterranean coastal sources): 25−30 $\mu g \cdot m^{-3}$
- Weekend effect: 15 $\mu g \cdot m^{-3}$

Considering the three episodes, on the four days of extraordinary exceedances in the city, a convergence of factors consistently occurred. These factors encompass weekend occurrences, multiregional convergence involving polluted air masses from at least two of the previously mentioned three source areas, and a Tramontana meteorological situation, among others.

S5. Photochemical model configuration

The model configuration can be found in Torre-Pascual et al. (2023) and the specifics for the simulations in this study are shown below.

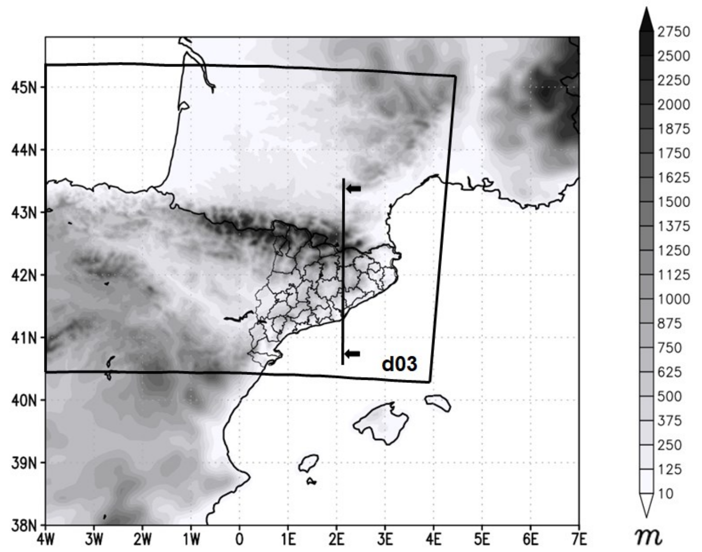

Figure S18. Spatial simulated coverage shown in the manuscript within d02 (9 km) – Iberian Peninsula – and partial view of the domain d03 (3 km) – Northern Iberian Peninsula – on its topographic map. The line shows the extension of the atmospheric cross-section analysed in Barcelona.

Table S1. Defined vertical levels for the WRF simulation and correspondence with, CAMx levels.

RF level number	CAMx level number	WRF η level	Approximate height of the CAMx layer interface (m above ground level)
1	1	1	Surface
2	2	0.9975	20
3	3	0.9950	40
4	4	0.9925	60
5	5	0.9900	80
6	6	0.9875	100
7	7	0.9850	120
8	8	0.9800	150
9	9	0.9700	235
10	10	0.9550	355
11	11	0.9400	480
12	12	0.9250	590
13	13	0.9100	730
14	14	0.8950	850
15	15	0.8800	1,000
16	16	0.8650	1,100
17	17	0.8500	1,250
18	18	0.8350	1,400
19	19	0.8200	1,500
20	20	0.8050	1,650
21	21	0.7900	1,800
22	22	0.7750	1,900

23	23	0.7600	2,000
24	24	0.7450	2,200
25	25	0.7300	2,400
26	26	0.7150	2,500
27	27	0.7000	2,700
28	28	0.6850	2,800
29	29	0.6700	2,950
30	30	0.6550	3,100
31	31	0.6400	3,300
32	32	0.6250	3,500
33	33	0.6100	3,650
34	34	0.5950	3,800
35	35	0.5800	4,000
36	36	0.5650	4,150
37	37	0.5500	4,300
38	38	0.5350	4,500
39	39	0.5200	4,700
40	40	0.5000	4,900
41	41	0.4800	5,200
42	42	0.4600	5,500
43	43	0.4400	5,750
44	44	0.4200	6,000

Table S2. Summary of WRF parameterizations.

Parameter	Option
Shortwave Radiation	MM5 Shortwave radiation scheme (Dudhia, 1989)
Longwave Radiation	Rapid Radiative Transfer Model (RRTM) (Mlawer et al., 1997)
Surface Model	Noah LSM (Alapaty et al., 2008)
Microphysics	WSM6 (Hong & Lim, 2006)
PBL	Yonsei University (YSU) (Hong, Noh & Dudhia, 2006)
SST	OISST (Reynolds et al., 2007)

Table S3. Spatial characteristics of the domains used in WRF and CAMx.

Domain	Spatial Resolution	WRF Number of grids	CAMx Number of grids
d01	27 km × 27 km	162 × 162	160 × 160
d02	9 km × 9 km	195 × 150	193 × 148
d03	3 km × 3 km	393 × 186	389 × 182

S6. Performance of the photochemical model simulations

In this section, the outcomes of the photochemical model validation are presented. For each episode, we quantified the performance of O_3 concentration model simulations at ground level in comparison to the observations at air quality stations. Our focus was on evaluating the model's performance in the study area including Barcelona and the surrounding areas (see stations and information in Figure 1 in the main manuscript). We have calculated the following statistical parameters: Mean Bias (MB), Mean Error (ME), Index of Agreement (IOA), and Pearson correlation coefficient (r), shown in Table S4, covering the periods indicated in the main manuscript. These parameters are commonly used for model validation.

Table S4. Statistical metrics used for the validation of the photochemical model

Metrics for validation	Equation
Mean Bias (MB)	$\frac{1}{N}\sum_{i=1}^{N}(Model_i - Obs_i)$
Mean Error (ME)	$\frac{1}{N}\sum_{i=1}^{N}\lvert Model_i - Obs_i\rvert$
Root Mean Square Error (RMSE)	$\sqrt{\frac{1}{N}\sum_{i=1}^{N}(Model_i - Obs_i)^2}$
Index of Agreement (IOA)	$1 - \frac{N \cdot \mathrm{RMSE}^2}{\sum_{i=1}^{N}(\lvert Model_i - \overline{Obs}\rvert + \lvert Obs_i - \overline{Obs}\rvert)^2}$
Pearson correlation coefficient (r)	$\frac{\sum_{i=1}^{N}(Model_i - \overline{Model}) \cdot (Obs_i - \overline{Obs})}{\sqrt{\sum_{i=1}^{N}(Model_i - \overline{Model})^2} \cdot \sqrt{\sum_{i=1}^{N}(Obs_i - \overline{Obs})^2}}$

For each episode, we present a set of figures containing the most significant outcomes: the spatial distribution of the statistical parameters for each station, and the violin plots showing their distribution.

The distribution and values of the statistical parameters for the three episodes are similar, and are within the metrics established in other photochemical modelling studies (Bessagnet et al., 2016; Oikonomakis et al., 2018). The median Pearson correlation coefficient (r) for all stations was 0.75, 0.71 and 0.66 for years 2015, 2018 and 2019, respectively; and the median Index of Agreement (IOA) was 0.78, 0.76 and 0.79. The CAMx model tends to underestimate O_3 concentrations for this region, with median MB of -3.81 (2015), -9.40 (2018) and -6.01 (2019). However, we see different spatial distributions on MB. Stations located in Barcelona, in the urban area, show a more pronounced underestimation, with MB values up to -40 $\mu g \cdot m^{-3}$. The low resolution of the emissions (0.1° × 0.1°) employed in this simulation make the urban emissions of NOx from Barcelona to be homogeneously distributed over the simulated cells close to the city, and therefore, the model reproduces greater O_3 titration. On the contrary, in the stations around Barcelona, the performance is significantly better, with MB values closer to zero and lower Mean Error (ME).

Episode 2015

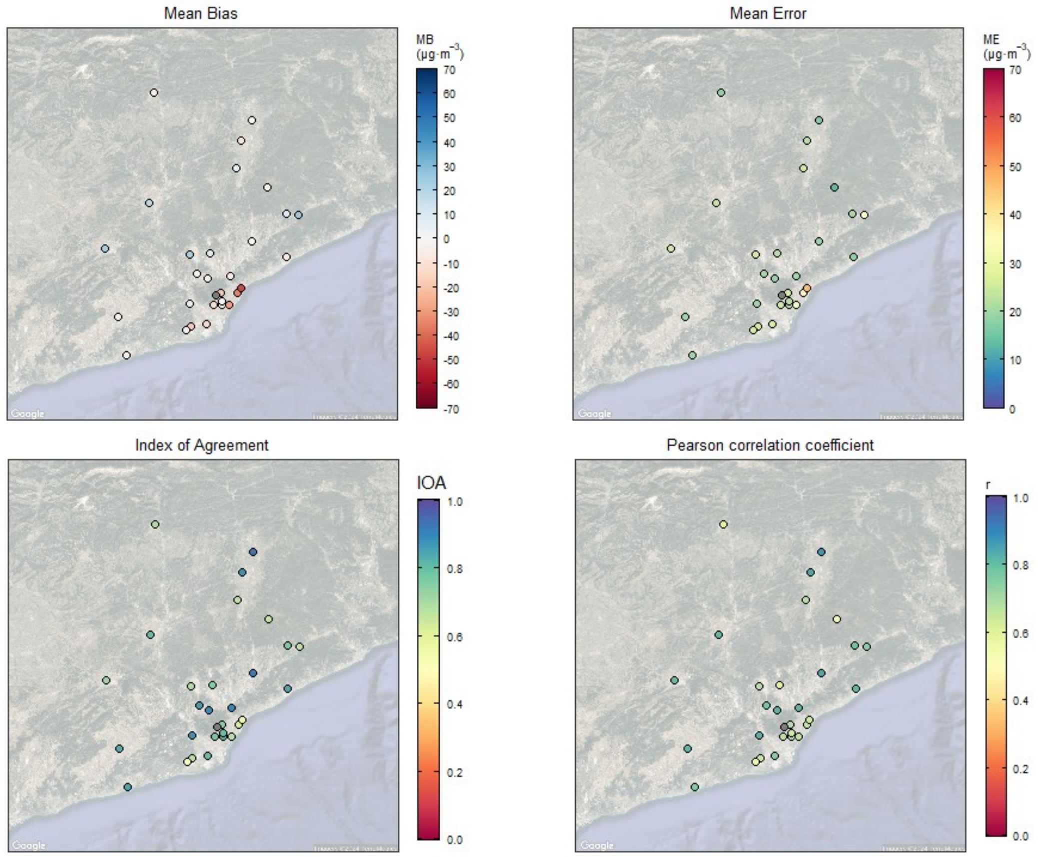

Figure S19. Spatial distribution of the Mean Bias (MB), Mean Error (ME), Index of Agreement (IOA), and Pearson correlation coefficient (r) values for the 2015 episode. (© Google Maps 2023)

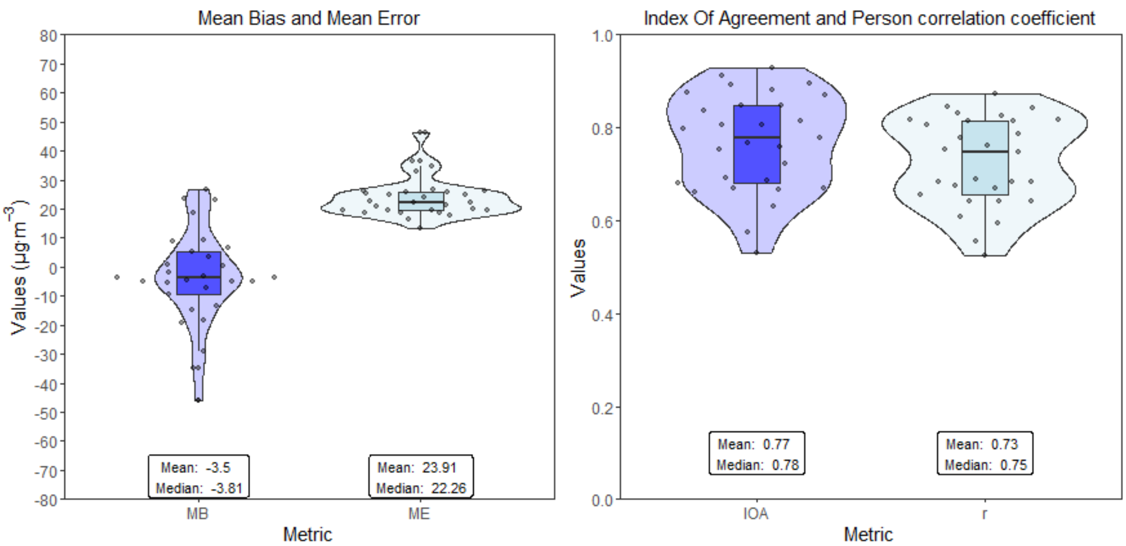

Figure S20. Violin plots for statistical metrics (MB, ME, IOA, and r) calculated for the O_3 monitoring stations for the 2015 episode. The boxes span from the first to the third quartile and the line inside the boxes represents the median. Whiskers extend within 1.5 times the interquartile range. Each point represents a single station and the curved lines represent the distribution shape of the data.

Episode 2018

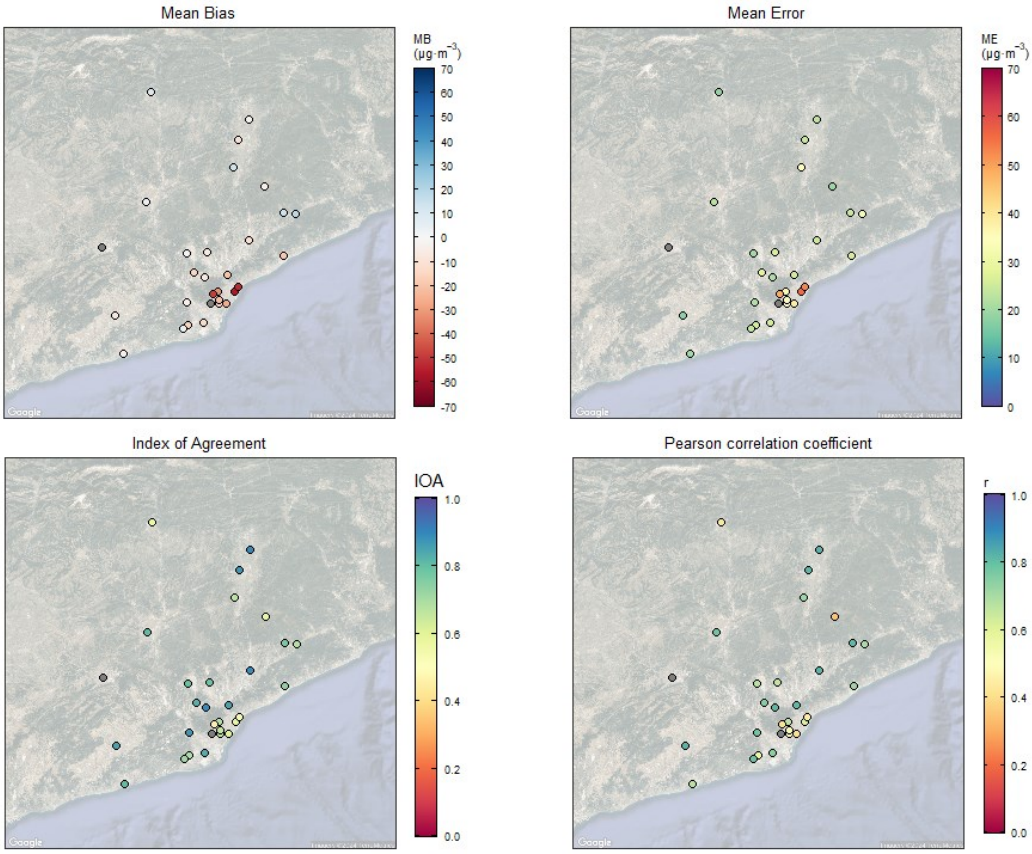

Figure S21. Spatial distribution of the Mean Bias (MB), Mean Error (ME), Index of Agreement (IOA), and Pearson correlation coefficient (r) values for the 2018 episode. (© Google Maps 2023)

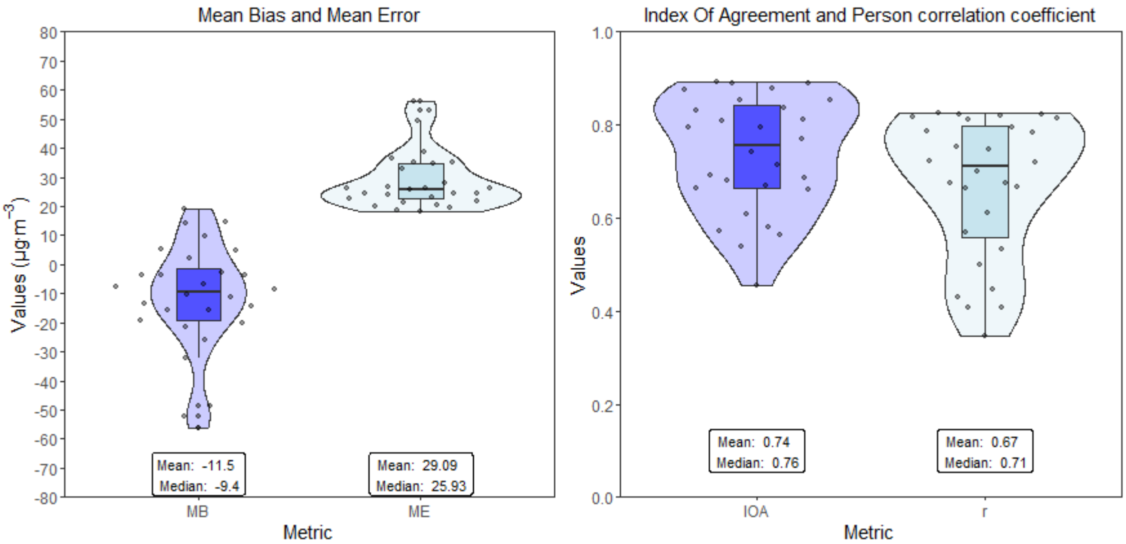

Figure S22. Violin plots for statistical metrics (MB, ME, IOA, and r) calculated for the O_3 monitoring stations for the 2018 episode. The boxes span from the first to the third quartile and the line inside the boxes represents the median. Whiskers extend within 1.5 times the interquartile range. Each point represents a single station and the curved lines represent the distribution shape of the data.

Episode 2019

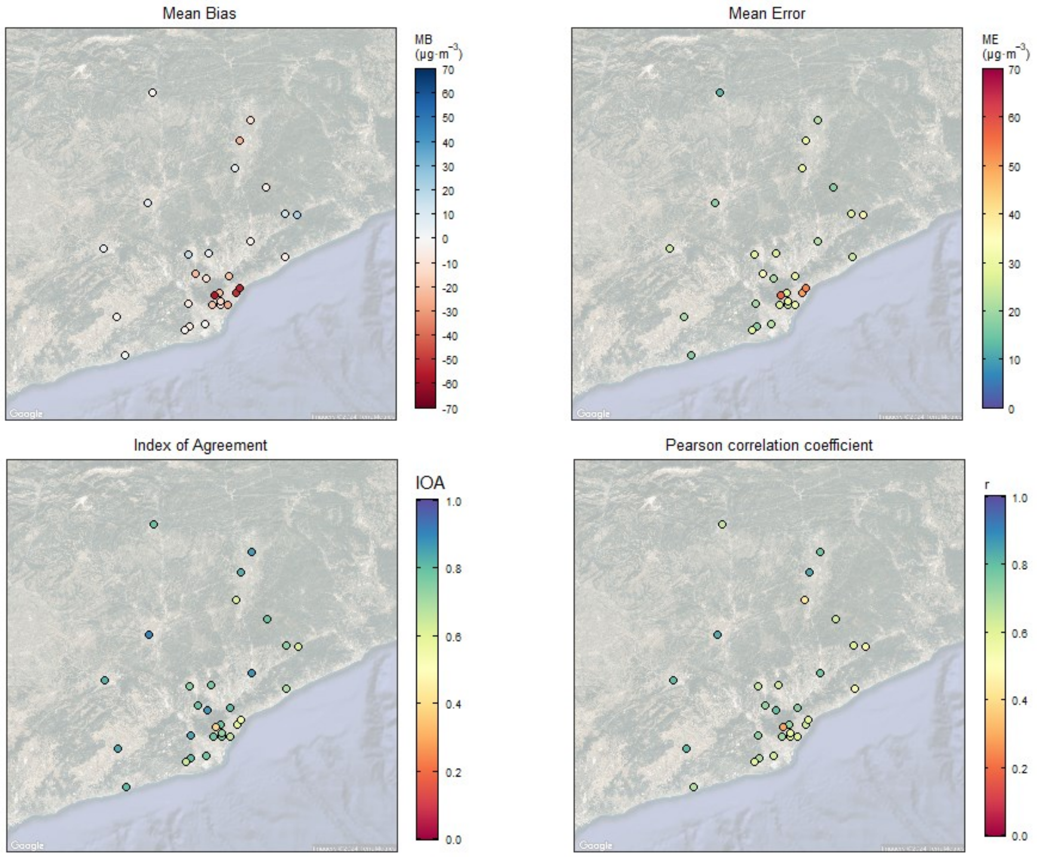

Figure S23. Spatial distribution of the Mean Bias (MB), Mean Error (ME), Index of Agreement (IOA), and Pearson correlation coefficient (r) values for the 2019 episode. (© Google Maps 2023)

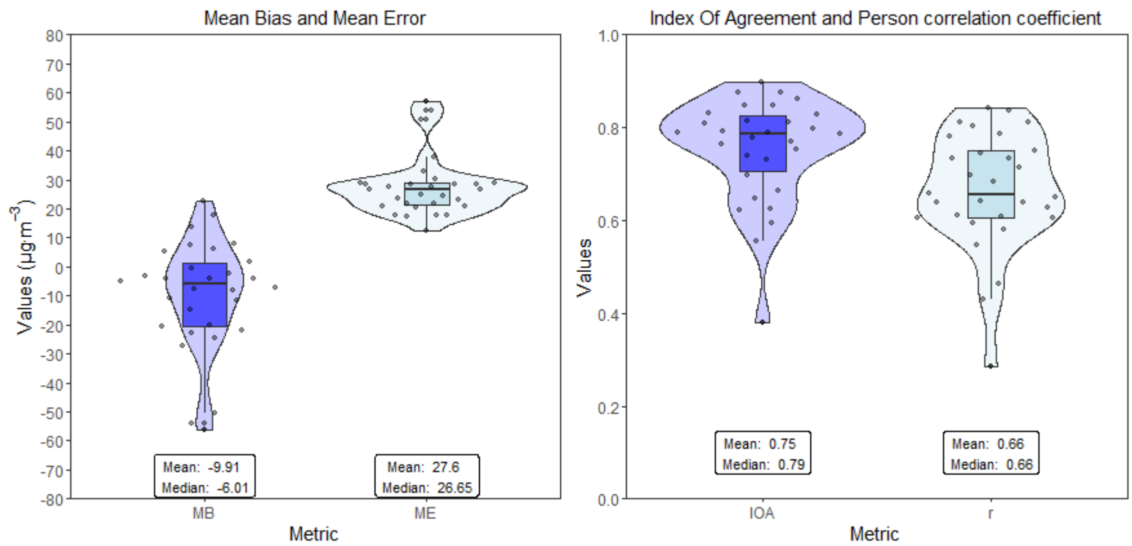

Figure S24. Violin plots for statistical metrics (MB, ME, IOA, and r) calculated for the O_3 monitoring stations for the 2019 episode. The boxes span from the first to the third quartile and the line inside the boxes represents the median. Whiskers extend within 1.5 times the interquartile range. Each point represents a single station and the curved lines represent the distribution shape of the data.

References

Alapaty, K., Niyogi, D., Chen, F., Pyle, P., Chandrasekar, A., and Seaman, N.: Development of the Flux-Adjusting Surface Data Assimilation System for Mesoscale Models, Journal of Applied Meteorology and Climatology, 47(9), 2331-2350, https://doi.org/10.1175/2008JAMC1831.1, 2008

Bessagnet, B., Pirovano, G., Mircea, M., Cuvelier, C., Aulinger, A., Calori, G., et al.: Presentation of the EURODELTA III intercomparison exercise – evaluation of the chemistry transport models' performance on criteria pollutants and joint analysis with meteorology, Atmospheric Chemistry and Physics, 16(19), 12667-12701, https://doi.org/10.5194/acp-16-12667-2016, 2016

Dudhia, J.: Numerical Study of Convection Observed during the Winter Monsoon Experiment Using a Mesoscale Two-Dimensional Model, Journal of the Atmospheric Sciences, 46(20), 3077-3107, https://doi.org/10.1175/1520-0469(1989)046<3077:NSOCOD>2.0.CO;2, 1989

Gangoiti, G., Millán, M. M., Salvador, R., and Mantilla, E.: Long range transport and recirculation of pollutants in the western Mediterranean during the project Regional Cycles of Air Pollution in the West-Central Mediterranean Area, Atmos. Environ., 35, 6267–6276, 2001

Hong, S. and Lim, J.: The WRF Single-Moment 6-Class Microphysics Scheme (WSM6), Journal of the Korean Meteorological Society, 42, 129-151, 2006

Hong, S.-Y., Noh, Y., and Dudhia, J.: A New Vertical Diffusion Package with an Explicit Treatment of Entrainment Processes, Monthly Weather Review, 134, 2318-2341, http://dx.doi.org/10.1175/MWR3199.1, 2006

Mlawer, E. J., Taubman, S. J., Brown, P. D., Iacono, M. J., and Clough, S. A.: Radiative transfer for inhomogeneous atmospheres: RRTM, a validated correlated-k model for the longwave, Journal of Geophysical Research: Atmospheres, 102(D14), 16663-16682, https://doi.org/10.1029/97JD00237, 1997

Oikonomakis, E., Aksoyoglu, S., Ciarelli, G., Baltensperger, U., and Prévôt, A. S. H.: Low modeled ozone production suggests underestimation of precursor emissions (especially NOx) in Europe, Atmospheric Chemistry and Physics, 18(3), 2175-2198, https://doi.org/10.5194/acp-18-2175-2018, 2018

Reynolds, R. W., Smith, T. M., Liu, C., Chelton, D. B., Casey, K. S., and Schlax., M. G.: Daily high-resolution-blended analyses for sea surface temperature, Journal of Climate, 20, 5473–5496, http://doi:10.1175/JCLI-D-14-00293.1, 2007

Torre-Pascual, E., Gangoiti, G., Rodríguez-García, A., Sáez de Cámara, E., Ferreira, J., Gama, C., Gómez, M. C., Zuazo, I., García, J. A., and de Blas, M.: Analysis of an intense O_3 pollution episode in the Atlantic Coast of the Iberian Peninsula using photochemical modelling: characterization of transport pathways and accumulation processes, EGUsphere [preprint], https://doi.org/10.5194/egusphere-2023-387, 2023